ADVANCED MATERIALS
www.advmat.de

Ultrafast Electrical Pulse Synthesis of Highly Active Electrocatalysts for Beyond-Industrial-Level Hydrogen Gas Batteries

*Taoli Jiang, Zaichun Liu, Yuan Yuan, Xinhua Zheng, Sunhyeong Park, Shuyang Wei, Linxiang Li, Yirui Ma, Shuang Liu, Jinghao Chen, Zhengxin Zhu, Yahan Meng, Ke Li, Jifei Sun, Qia Peng, and Wei Chen**

The high reliability and proven ultra-longevity make aqueous hydrogen gas (H_2) batteries ideal for large-scale energy storage. However, the low alkaline hydrogen evolution and oxidation reaction (HER/HOR) activities of expensive platinum catalysts severely hamper their widespread applications in H_2 batteries. Here, cost-effective, highly active electrocatalysts, with a model of ruthenium-nickel alloy nanoparticles in ≈3 nm anchored on carbon black (RuNi/C) as an example, are developed by an ultrafast electrical pulse approach for nickel-hydrogen gas (Ni–H_2) batteries. Having a competitive low cost of about one fifth of Pt/C benckmark, this ultrafine RuNi/C catalyst displays an ultrahigh HOR mass activity of 2.34 A mg^{-1} at 50 mV (vs RHE) and an ultralow HER overpotential of 19.5 mV at a current density of 10 mA cm^{-2}. As a result, the advanced Ni–H_2 battery can efficiently operate under all-climate conditions (from −25 to +50 °C) with excellent durability. Notably, the Ni–H_2 cell stack achieves an energy density up to 183 Wh kg^{-1} and an estimated cost of ≈49 $ kWh^{-1} under an ultrahigh cathode $Ni(OH)_2$ loading of 280 mg cm^{-2} and a low anode Ru loading of ≈62.5 µg cm^{-2}. The advanced beyond-industrial-level hydrogen gas batteries provide great opportunities for practical grid-scale energy storage applications.

1. Introduction

Currently, there is an urgent call for battery energy storage technologies to mitigate the intrinsic intermittency of renewables in the future grid.[1] Considering the demand for all-year-round stable supply and low price of electricity, the ultralow levelized cost of storage and high reliability are critical requirements for the grid-scale energy storage.[1a] For this purpose, battery technologies of long cycle life, low-cost, all-climate feasibility, high energy efficiency (EE), and risk-free security are critical requirements to fulfill. The existing battery technologies, including lithium-ion batteries, molten-salt batteries, vanadium redox-flow batteries, and lead-acid batteries, can hardly meet the criteria due to their potential safety issues, high initial cost, or insufficient cycle life.[2] Alternatively, some emerging battery technologies such as aqueous metal-ion batteries show unsatisfied energy density and immature industrial development.[3]

Rechargeable hydrogen gas batteries have been attracting significant research and industrial interests owing to their unprecedent long-term cycle stability, high reliability, and competitive low cost, rendering them ideal for large-scale energy storage. The technology-proven Ni-H_2 battery has been deployed as a unique energy storage system in satellites and aerospace stations since the 1970s for over 30 years of service life with guaranteed safety.[4] For instance, the ground testing of Ni–H_2 batteries at Eagle-Picher has verified a life of more than 100 000 charge/discharge cycles.[4] Therefore, the highly reliable and ultralong life aqueous Ni–H_2 batteries have been considered as a highly attractive technology for the grid-scale energy storage. The Ni–H_2 batteries are operated by the cathode nickel hydroxide/oxyhydroxide ($Ni(OH)_2$/NiOOH) conversion reactions and the anode electrocatalytic hydrogen evolution/oxidation reactions (HER/HOR) in alkaline electrolytes.[5] The $Ni(OH)_2$/NiOOH redox couple has been widely used as a robust cathode in commercialized alkaline batteries.[2,6] At the anode, H_2 evolves from the alkaline electrolyte during charge and is oxidized to H_2O during discharge.[7] Interestingly, the HER/HOR anode possesses an ultrahigh specific capacity of 2978 mAh $g_{(water)}^{-1}$ and is free of direct wear-out mechanism.[4,8] However, the HER/HOR activities of platinum group metals (PGMs) drop ≈100-fold when changing the electrolyte from acid to base.[8] The sluggish alkaline HER/HOR kinetics of PGMs typically requires Pt loading >0.5 mg cm^{-2} in conventional hydrogen

T. Jiang, Z. Liu, Y. Yuan, X. Zheng, S. Park, S. Wei, L. Li, Y. Ma, S. Liu, J. Chen, Z. Zhu, Y. Meng, K. Li, J. Sun, Q. Peng, W. Chen
Department of Applied Chemistry
School of Chemistry and Materials Science
Hefei National Research Center for Physical Sciences at the Microscale
University of Science and Technology of China
Hefei, Anhui 230026, China
E-mail: weichen1@ustc.edu.cn

The ORCID identification number(s) for the author(s) of this article can be found under https://doi.org/10.1002/adma.202300502

DOI: 10.1002/adma.202300502

anodes for space missions, which are unaffordable for grid-scale energy storage applications.[4,9] The renaissance of Ni–H_2 battery technology by developing low-cost, durable, and highly active alkaline HER/HOR bifunctional catalysts to replace Pt is of great significance.

In previous studies, Chen et al. synthesized a cost-effective nickel-molybdenum-cobalt anode by an electrochemical deposition method, which demonstrated excellent electrochemical performance at low charge and discharge rates for Ni–H_2 battery.[7] However, the mass activity of non-noble catalysts need further improvement for high rate performance of Ni–H_2 battery.[10,11] Ru is one of the cheapest PGMs with one-third average price of Pt in the past five years and has attracted extensive attention in the fuel cell industry recently.[12] The Ru-based alloying strategies have been demonstrated to be a very effective way to achieve higher alkaline HER/HOR activity than the benchmark Pt.[12,13] However, the Ru-based catalysts are still not widely used to industrial fuel cells, which require high power density . The reason is that the Ru-based catalysts are susceptible to oxidation and thus loss of activity at an anode potential of more than 100 mV versus RHE.[12] Nevertheless, this is not an issue for the H_2 battery energy storage application, because it only requires a sufficiently low overpotential to drive the reversible HER/HOR. Therefore, the Ru-based catalysts in the H_2 battery can be well maintained for long-term durability. There are various routines including template methods and solvothermal methods to synthesize highly active PGM-based electrocatalysts (such as nanowires, nanosheets, and nanocages).[14] However, these methods generally display low yield and the catalysts can hardly be mass produced. The thermal treatment is an important industrial approach to achieve metal nanocatalysts from the metal salt precursors. However, the conventional thermal treatment methods typically show low energy utilization efficiencies (<10%), long synthesis duration (>1 h), and slow heating/cooling rates (<100 K min^{-1}). The slow heating/cooling rates are prone to generate uneven reaction conditions, which result in nanoparticle aggregation.[15] Therefore, it is important to develop an energy-saving, fast-rate, and effective preparation approach to the fabrication of Ru-based nanocatalysts for Ni–H_2 battery energy storage applications.

Here, we utilize a facile and ultrafast electrical pulse method to develop highly active electrocatalysts for the beyond-industrial-level H_2 battery energy storage applications. With a competitive cost of ≈1/5 of the benchmark Pt/C catalyst, the RuNi/C catalyst displays excellent HOR mass activities, which are 7.5 and 10 times higher than the commercial Pt/C and Ru/C at 50 mV in 0.1 M KOH, respectively. Meanwhile, it shows a low HER overpotential of 19.5 mV at a current density of 10 mA cm^{-2}, which is much better than 32 mV for Pt/C and 48 mV for Ru/C. The Ni–H_2 (RuNi) battery by employing RuNi/C as the H_2 catalyst shows a higher EE than the Ni–H_2 (Pt) battery, and the former exhibits excellent durability with negligible decay over 1500 cycles. In addition, the Ni–H_2 (RuNi) battery can efficiently operate in the all-climate temperature range (−25–50 °C). Excitingly, under an ultralow ruthenium loading of ≈62 μg_{Ru} cm^{-2} for the anode and an ultrahigh areal $Ni(OH)_2$ loading of 280 mg cm^{-2} (60 mAh cm^{-2}) for the cathode, the assembled Ni–H_2 (RuNi) battery achieves a high cell-level energy density of 183 Wh kg^{-1} with a high energy efficiency of >85%. The estimated cost of the Ni–H_2 (RuNi) battery stack reaches as low as ≈\$49.1 kWh^{-1}. A scaled-up Ah-level Ni–H_2 (RuNi) battery is further assembled for practical demonstration. Benefiting from the excellent comprehensive performance and potential economic advantages of RuNi/C by the facile and ultrafast electrical pulse method, this work shows the development of practical, beyond-industrial-level, and high-performance hydrogen gas batteries for grid-scale energy storage.

2. Results and Discussion

The RuNi/C catalysts were synthesized by an ultrafast electrical pulse method in Ar atmosphere within 0.5 s (**Figure 1**a,b; Figure S1, Supporting Information). First, commercial Vulcan XC72 was mildly oxidized with nitric acid to introduce oxygenated functional groups on the surface. With abundant carboxylic acids, Ru^{3+} and Ni^{2+} can be easily adsorbed on Vulcan XC72 by forming Ru–Ni carboxylate complexes. Then, the complexes were placed between two tightly attached carbon cloths and the working temperature of the carbon cloths was adjusted by the input current of the direct-current power supply. During the electrical pulse process, the high temperature rapidly reduced the metal ion into metal nanoparticles, which were tightly anchored on the carbon black and then cooled rapidly to prevent nanoparticle agglomeration.[15] The morphology, elemental mapping, and particle size of the catalyst were explored by transmission electron microscopy (TEM). The TEM images clearly showed that the RuNi nanoparticles were uniformly anchored onto the carbon black substrates (Figure 1c; Figure S2a, Supporting Information). Thanks to the ultrafast heating/cooling rates, the RuNi particle size was distributed in the range of 1–5 nm, and the average size was ≈3 nm (Figure S2b, Supporting Information). The high-resolution TEM (HRTEM) images of RuNi nanoparticles are shown in the inset of Figure 1c, in which the lattice fringes with a spacing of ≈0.203 nm correspond to the (101) plane of the Ru-based catalysts (Figure S3, Supporting Information). The slightly smaller lattice fringe for Ru compared to that of bulk Ru (0.206 nm) is caused by the incorporation of Ni. The elemental mapping under energy dispersive X-ray spectroscopy (EDS) indicates the high spatial correlation between Ru, Ni, and O species and thereby suggests the formation of a uniform alloy with slight oxidation (Figure 1d,e). The EDS line-scanning profile (Figure 1f) further confirmed the alloying effect, in which Ni and O are accompanied by Ru elements. The metal content of the RuNi/C catalyst is proven by thermogravimetry (TG) results of 7.5 wt% (Figure S4, Supporting Information).

The X-ray diffraction (XRD) patterns of the RuNi/C catalysts are shown in Figure S5 (Supporting Information), indicating that the catalysts are mainly composed of RuNi alloy, which has similar peaks to hexagonal close-packed (hcp) Ru. X-ray photoelectron spectroscopy (XPS) analysis was further carried out to investigate the detailed elemental composition and surface chemical state of the sample. As shown in Figure S6 (Supporting Information), the Ru 3d XPS spectra can be deconvoluted into four peaks. The two main peaks located at 280.7 and 285.3 eV can be assigned to Ru^0 $3d_{5/2}$ and Ru^0 $3d_{3/2}$, respectively, and the two shoulder peaks at 282.1 and 286.4 eV correspond to Ru^{4+} $3d_{5/2}$ and Ru^{4+} $3d_{3/2}$, respectively. This result suggests that Ru is partially oxidized, but the majority is still in the metallic state. The Ru 3p XPS spectra of commercial Ru/C and RuNi/C were also

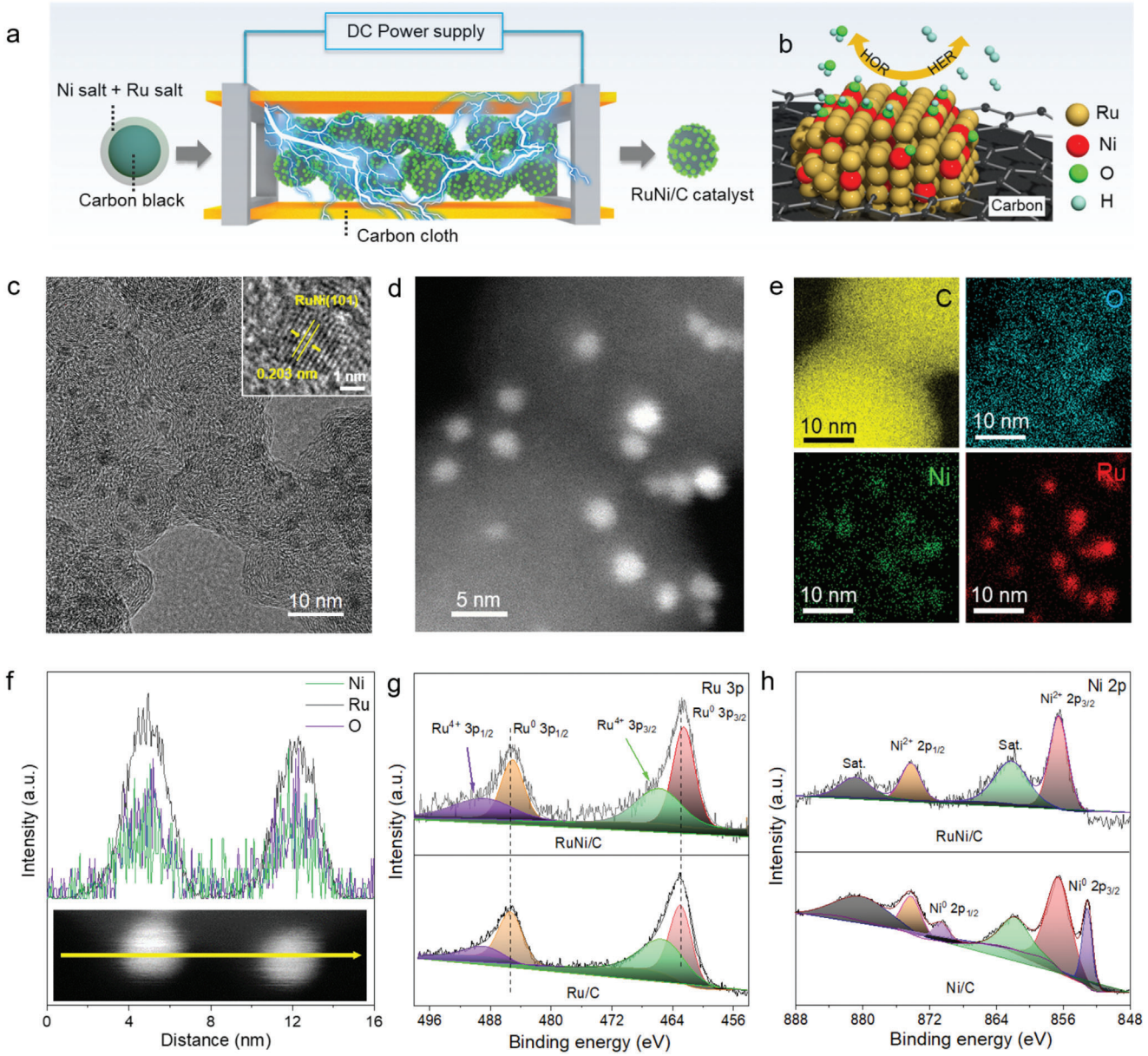

Figure 1. Characterization of the RuNi/C catalysts. a) Schematic illustration of the electrical pulse synthesis of RuNi/C catalyst. b) Schematic illustration of RuNi/C for HER/HOR. c) TEM and HRTEM images of RuNi/C. d) High-angle annular dark-field scanning transmission electron microscopy (HAADF-STEM) images and e) the corresponding elemental mapping images of the RuNi/C catalyst. f) EDS line-scanning profile of RuNi/C, inset: HAADF-STEM image showing the corresponding line scanned area. g) Ru 3p XPS spectra of RuNi/C and commercial Ru/C catalysts. h) Ni 2p XPS spectra of RuNi/C and Ni/C catalysts.

shown in Figure 1g. Two similar main peaks located at 462.5 eV and 485.0 eV can be assigned to Ru^0 $2p_{3/2}$ and Ru^0 $2p_{1/2}$, respectively, which revealed that commercial Ru/C was also inevitably partially oxidized. Compared with that of commercial Ru/C, the Ru^0 3p binding energy of RuNi/C showed a negative shift of ≈0.4 eV, suggesting that Ru was further accommodated electrons due to the Ni doping effect.[12] Figure 1h shows the Ni 2p XPS spectra of RuNi/C and Ni/C. The Ni $2p_{3/2}$ peaks at 853.0 eV and 856.5 eV are attributed to Ni^0 and Ni^{2+}, respectively. It is found that the Ni element on the surface of RuNi/C is completely oxidized.

The catalytic activities of RuNi/C toward bifunctional HER/HOR were first characterized in a standard three-electrode system with a glassy carbon rotating disk electrode (RDE) in the H_2-saturated 0.1 M KOH electrolyte. The Ru/Ni atomic ratios of Ru_xNi_y/C were confirmed by inductively coupled plasma optical emission spectroscopy (ICP–OES). The optimal Ru/Ni ratio of Ru_xNi_y/C for HER/HOR catalysis was tested to be ≈3/2 (Figure S7, Supporting Information). The metal cost of the Ru_3Ni_2/C catalyst is ≈1/5 of the benchmark Pt/C catalyst. The HOR polarization curves of the studied catalysts are shown in **Figure 2**a. Commercial Ni/C, Pt/C, and Ru/C with the same

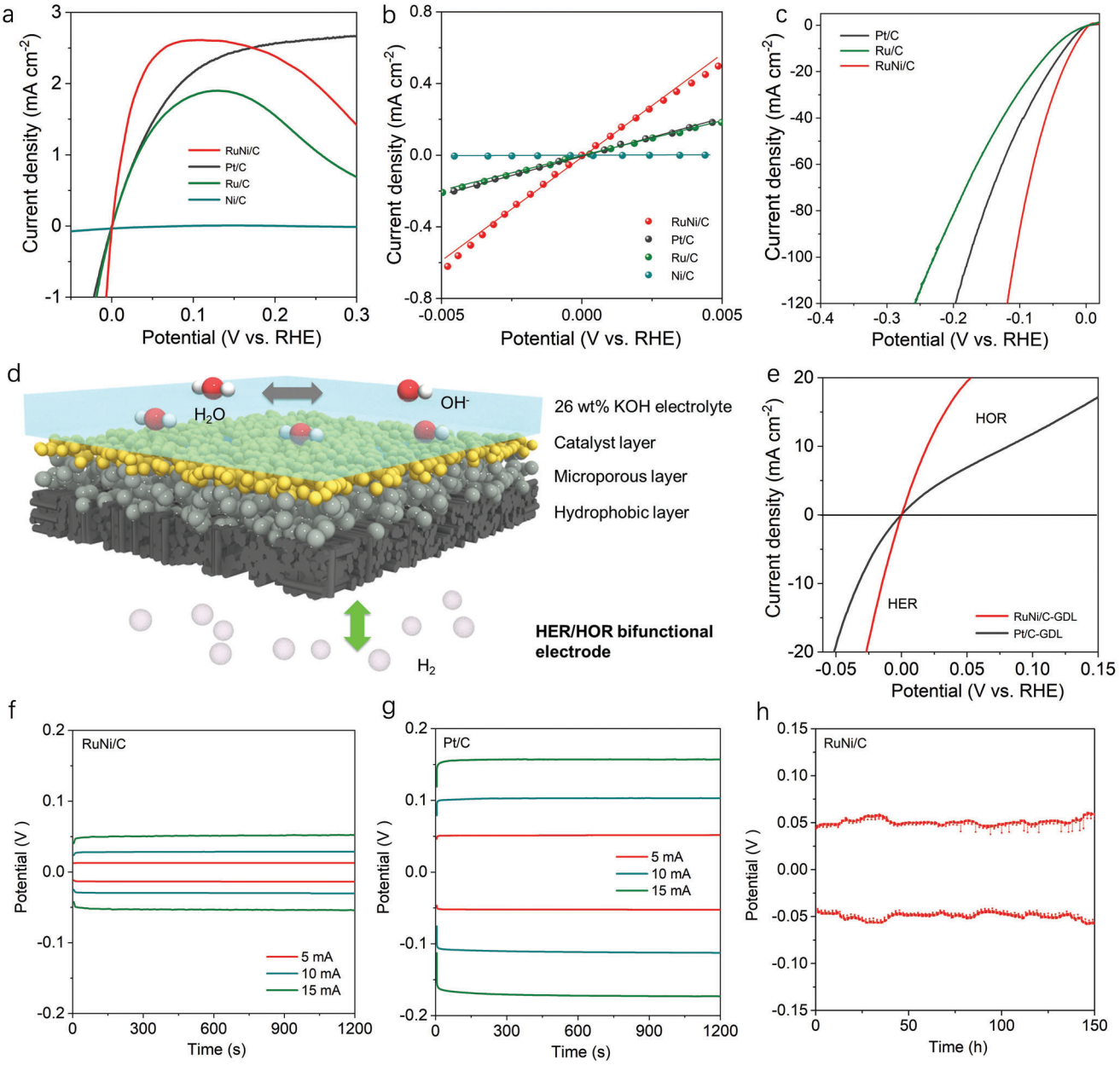

Figure 2. Hydrogen oxidation and evolution reaction activity tests. a) HOR polarization curves of RuNi/C, Pt/C, Ru/C, and Ni/C in H_2-saturated 0.1 M KOH with a scan rate of 5 mV s^{-1} at a rotating speed of 1600 rpm. b) Linear current potential region around the equilibrium potential of the HOR/HER of RuNi/C, Pt/C, Ru/C, and Ni/C. c) HER polarization curves of RuNi/C and Pt/C in Ar-saturated 1 M KOH. d) Schematic diagram of the H_2 electrode. e) HER/HOR polarization curves of RuNi/C-GDE and Pt/C-GDE. Galvanostatic cycling curves of the symmetric H_2 cells using RuNi/C-GDE (f) and Pt/C-GDE (g). h) Time-dependent voltage profiles of the symmetric H_2 cell using RuNi/C-GDE.

metal loading of ≈10 μg cm^{-2} were tested for comparison. The HOR current densities measured at 50 mV are 2.35, 1.47, and 1.36 mA cm^{-2} for RuNi/C, Pt/C, and Ru/C, respectively, while the Ni/C catalyst shows inertness for the HOR. The RuNi/C has a much smaller half-wave potential of 16.5 mV than Pt/C with 44 mV, which quickly reaches the diffusion-limited current at a low potential of 89 mV. The exchange current density (j_0) of HOR/HER was obtained from the micro-polarization region (Figure 2b), which deviates only several millivolts from the equilibrium potential.[16] The obtained j_0 value of RuNi/C is 3.11 mA cm^{-2}, which is much superior to that of Pt/C with a j_0 value of 1.01 mA cm^{-2}. The HOR polarization curves of RuNi/C under different electrode rotation rates are shown in Figure S8a (Supporting Information). The limiting current density grows with the rotating speed due to the promoted H_2 diffusion and mass transport. The Koutecky–Levich (K-L) plot is shown in Figure S8b (Supporting Information). A straight line was obtained with a slope of 4.56 cm^2 mA^{-1} $s^{-1/2}$, close to the theoretical value of 4.87 cm^2 mA^{-1} $s^{-1/2}$ for the two-electron HOR process. We further used the K–L equation to calculate the

kinetic current density (J_k) of the RuNi/C catalyst. At an overpotential of 50 mV, a geometric J_k of 16.42 mA cm^{-2} was obtained, which represents 5.2- and 7-fold increase compared with those of commercial Pt/C (3.12 mA cm^{-2}) and Ru/C (2.32 mA cm^{-2}) catalysts (Figures S9 and S10, Supporting Information), respectively. The mass-normalized J_k reflects the economy of the synthesized catalysts based on weight. The mass-normalized J_k values of the RuNi/C, commercial Ru/C and Pt/C catalysts are shown in Figure S11 (Supporting Information). The RuNi/C catalysts have an ultrahigh mass activity of 2.34 A $mg_{Ru}{}^{-1}$, which is 7.5 and 10 times higher than that of commercial Pt/C (0.31 A $mg_{Pt}{}^{-1}$) and Ru/C (0.23 A $mg_{Ru}{}^{-1}$), respectively. The HER polarization curves of RuNi/C, Ru/C, and Pt/C in 1 M KOH electrolyte are shown in Figure 2c, exhibiting that it only needs an overpotential of 19.4 mV for RuNi/C to deliver a current density of 10 mA cm^{-2}, which is better than 32 mV for Pt/C and 48 mV for Ru/C. It is summarized that our as-synthesized RuNi/C catalysts exhibit superior HER/HOR activities to most of the previously reported PGM catalysts (Table S1, Supporting Information).

Based on the excellent HER/HOR activities of RuNi/C, we prepared a hydrogen catalytic electrode by coating the catalyst on a gas diffusion electrode (GDE). A schematic diagram of the hydrogen electrode is shown in Figure 2d. The hydrophobic layer is conducive to H_2 transport for the HOR process. The HER/HOR reversibility of RuNi/C-GDE and Pt/C-GDE was conducted in a H_2-saturated 26 wt.% KOH electrolyte. As shown in Figure 2e, the RuNi/C-GDE with excellent HER/HOR activities significantly reduced the accumulative HER and HOR overpotential (54.1 mV) to deliver a current density of 15 mA cm^{-2} compared to Pt/C-GDE (173.2 mV). This indicates that the electrode can operate at a high current density and maintain a low overpotential to achieve the high energy efficiency for the H_2 battery. In addition, the H_2 symmetric cell is constructed by two pieces of GDE and a separator wetted with 26 wt.% KOH electrolytes. As shown in Figure 2f,g, the electrode polarization voltages of the H_2 symmetric cells were tested at current densities from 5 to 15 mA cm^{-2}, and the corresponding charge/discharge voltage hysteresis increased almost linearly with the current density. Obviously, the RuNi/C-GDE shows a lower polarization voltage of ≈51 mV than the Pt/C-GDE of >150 mV at a current density of 15 mA cm^{-2}. Furthermore, the time-dependent voltage profiles of the symmetric cells are shown in Figure 2h. The polarization voltages of the symmetric cell using RuNi/C at a current density of 15 mA cm^{-2} for both HER and HOR are stable at ≈50 mV for over 150 h, which shows excellent long-term HER/HOR bifunctional durability.

To gain insight into the origin of the RuNi alloying effect for the HER/HOR under alkaline conditions, density functional theory (DFT) calculations were performed to simulate the HER/HOR reaction pathways on Ru (101) and RuNi (101). The H_2O adsorption of the HER was first investigated, and the corresponding differential charge density color-filled optimized configurations are presented in **Figure 3**a and Figure S12 (Supporting Information). The surface edge Ru atoms are recognized as the H_2O adsorption sites, and obvious electronic interaction and electron rearrangement occurred after water adsorption on the edge Ru atoms of Ru (101) and RuNi (101). The H_2O molecules were activated after chemisorption, with an increase in the H–O bond length and a change in the partial density of states (PDOS) of H_2O (Figure 3c). The HER/HOR pathway on RuNi (101) and calculated free energy diagrams, including H_2O adsorption, H_2O dissociation, hydrogen adsorption, and hydrogen generation, are plotted in Figure 3b and Figure 3d to further understand the difference in the alkaline HER/HOR reversibility between Ru and RuNi catalysts. The highest free energy climb step during the reversible HER/HOR was normally considered as the rate-determining step (RDS). For RuNi (101), the step of desorption of *OH species in HER is identified as the RDS with a free energy climb of 0.41 eV, which is the last step of Volmer process.[17] For Ru (101), the desorption of *OH species during the HER is also the RDS, which is much difficult than that of RuNi (101) with a higher free energy climb of 0.71 eV. Moreover, it is worth mentioning that in HOR, the step of combining adsorbed *H and *OH to generate adsorbed *H_2O on Ru (101) is much more difficult than that on RuNi (101). Therefore, the above results show that RuNi (101) can enable a better reversible alkaline HER/HOR performance from the viewpoint of thermodynamics. Moreover, the energy barrier of water activation (E_a) was investigated by conducting climbing image nudged elastic band (CI-NEB) calculations (Figure 3e), which is generally considered as the kinetic barriers that could affect the overall reaction rates.[18] The reversible HER/HOR is expected to have much favorable kinetics on RuNi (101) with transition reaction barriers for H_2O dissociation/formation of 0.77 eV, which is much lower than the calculated H_2O dissociation/formation barrier on the Ru (101) surface of 1.32 eV. In short, the Ru atom on the surface of the RuNi alloy plays a key role in the entire HER/HOR path in alkaline solution. The Ni alloying optimized the electronic structure of Ru and accelerated the RDS of the HER/HOR. As a result, the intrinsic activities of HER/HOR at Ru sites were greatly improved.

A schematic diagram of the Ni-H_2 battery and its redox reactions during the charge and discharge is shown in **Figure 4**a. The Ni-H_2 battery was constructed with a H_2 GDE anode, a commercial $Ni(OH)_2$ cathode, and aqueous KOH solution as the electrolyte (Figure 4d).[19] Based on previous work, a concentration of 26 wt.% is beneficial in reducing the occurrence of $Ni(OH)_2$/NiOOH swelling in operation, thereby improving the cycle life of the cell.[19] The $Ni(OH)_2$ electrode (Figure S13, Supporting Information) with high areal capacity and tap density is known to be highly stable for commercial alkaline batteries, enabling our Ni-H_2 battery to reach industrial level requirements.[6] The SEM image shows the compactly packed $Ni(OH)_2$ cathode (Figure 4b), which is remarkably different from the porous and uniformly distributed RuNi/C nanocatalysts on the anode (Figure 4c). After the battery fabrication, the two charged Ni-H_2 Swagelok batteries connecting in series can light up a light emitting diode display screen with a power of 15 mW (Figure 4e).

Figure 4f shows the galvanostatic charge-discharge curves of the Ni-H_2 batteries, which are assembled by coupling the RuNi/C-GDE (0.121 mg_{Ru} cm^{-2}) anode or Pt/C-GDE (≈0.45 mg_{Pt} cm^{-2}) anode with a $Ni(OH)_2$ cathode (mass loading of 70 mg cm^{-2}, areal capacity of 15 mAh cm^{-2}), at a current density of 15 mA cm^{-2}. The Ni-H_2 (RuNi) battery shows a much lower overpotential than that of the Ni-H_2 (Pt) battery, where the former delivers a high energy efficiency of ≈86.5% as compared to the latter (≈75%). The Ni-H_2 (RuNi) battery exhibits excellent rechargeability with negligible decay of discharge

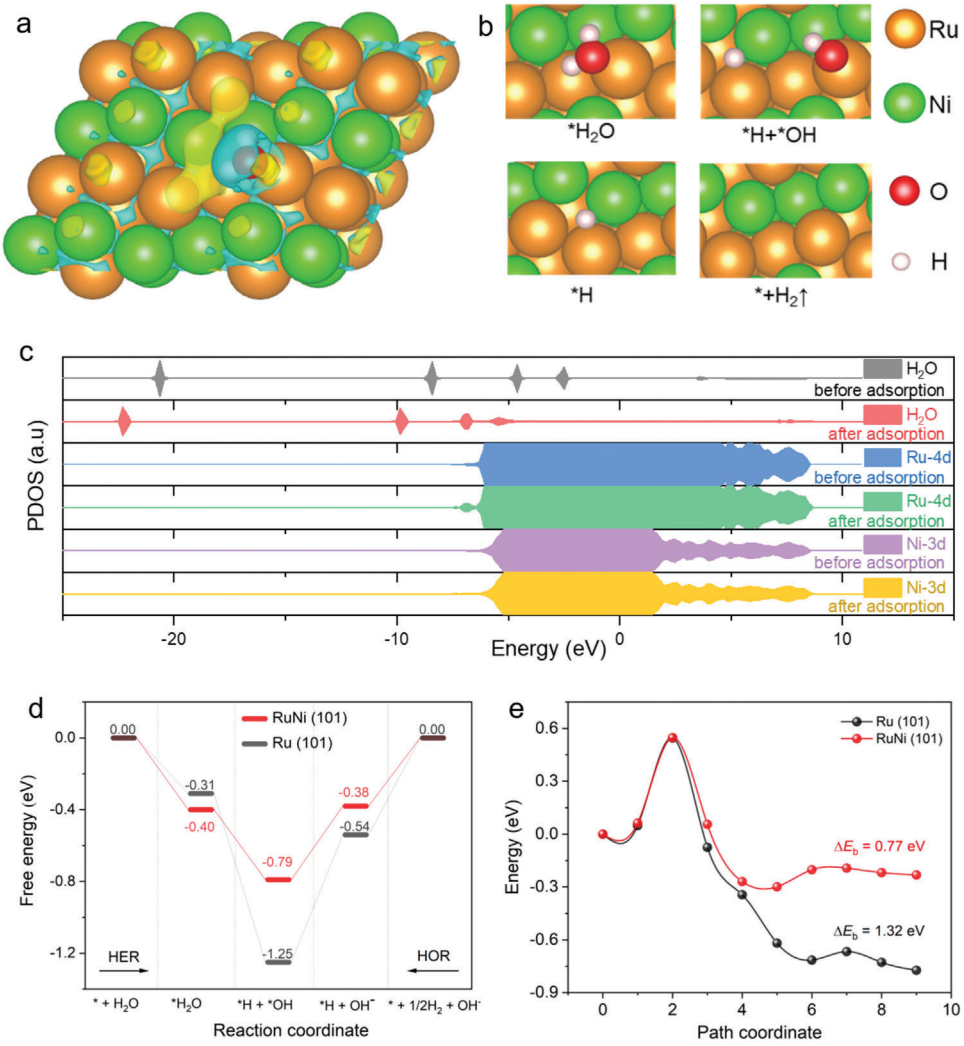

Figure 3. First-principles density functional theory calculations. a) Differential charge density of the H_2O-RuNi (101) structure. b) The alkaline HER/HOR pathway on RuNi (101). c) The PDOS of H_2O, Ru 4d, Ni 3d before and after adsorption. d) Calculated free energy versus the reaction coordinate of HER and HOR in simulated models of RuNi (101) and Ru (101). e) The energy barrier for water dissociation/formation on Ru (101) and RuNi (101).

capacity after 500 cycles (3000 h) at a current density of 5 mA cm^{-2} (Figure 4g). Figure S14 (Supporting Information) shows the largely overlapped 50th and 500th cycles of galvanostatic charge-discharge curves of the Ni-H_2 (RuNi) battery, implying its excellent durability. The slight EE decay from 88% to 86.5% is mainly due to the detachment of the cathode active materials, which can be observed from the SEM imaging (Figure S15, Supporting Information). The Ni-H_2 (RuNi) battery was also tested at various current densities with 66.7% depth of discharge (DoD) for rate performance. As the current density increases from 10 to 50 mA cm^{-2}, the Ni-H_2 battery still shows well-retained discharge capacities and slightly decreased voltage efficiency after 1500 cycles (Figure 4h,i). For example, a relatively high EE of > 75% can be achieved even at a high current density of 50 mA cm^{-2}. In contrast, the Ni-H_2 (Pt) battery demonstrates obviously worse rate performance and higher cost than that of the Ni-H_2 (RuNi) battery (Figure S16 and Table S2, Supporting Information). Meanwhile, the Ni-H_2 (RuNi) battery shows a high cell-level energy density of 130 Wh kg^{-1} and an estimated energy cost of 107.8 \$ kWh^{-1} based on the cell stack but excluding the Swagelok gas storage vessel (Table S3, Supporting Information).

Given the strict operational environment of grid-scale energy storage, we further studied the charge-discharge performance of the battery at temperatures from −25 to 50 °C (Figure 4j–l). Impressively, even at a low temperature of −25 °C, the Ni-H_2 (RuNi) battery still possessed well-retained 100% DoD capacities with only slightly decreased energy efficiency (≈86.5%) at 5 mA cm^{-2}, indicating its excellent low-temperature electrochemical performance (Figure 4j). Furthermore, the battery can work well at a high temperature of 50 °C with high energy efficiencies (>85%) at current densities from 15 to 45 mA cm^{-2} in 80% DoD (Figure 4l). Consequently, the Ni-H_2 (RuNi) battery can efficiently operate at a wide temperature range, which covers most residential areas on the Earth, demonstrating the all-climate capability of our hydrogen gas batteries.

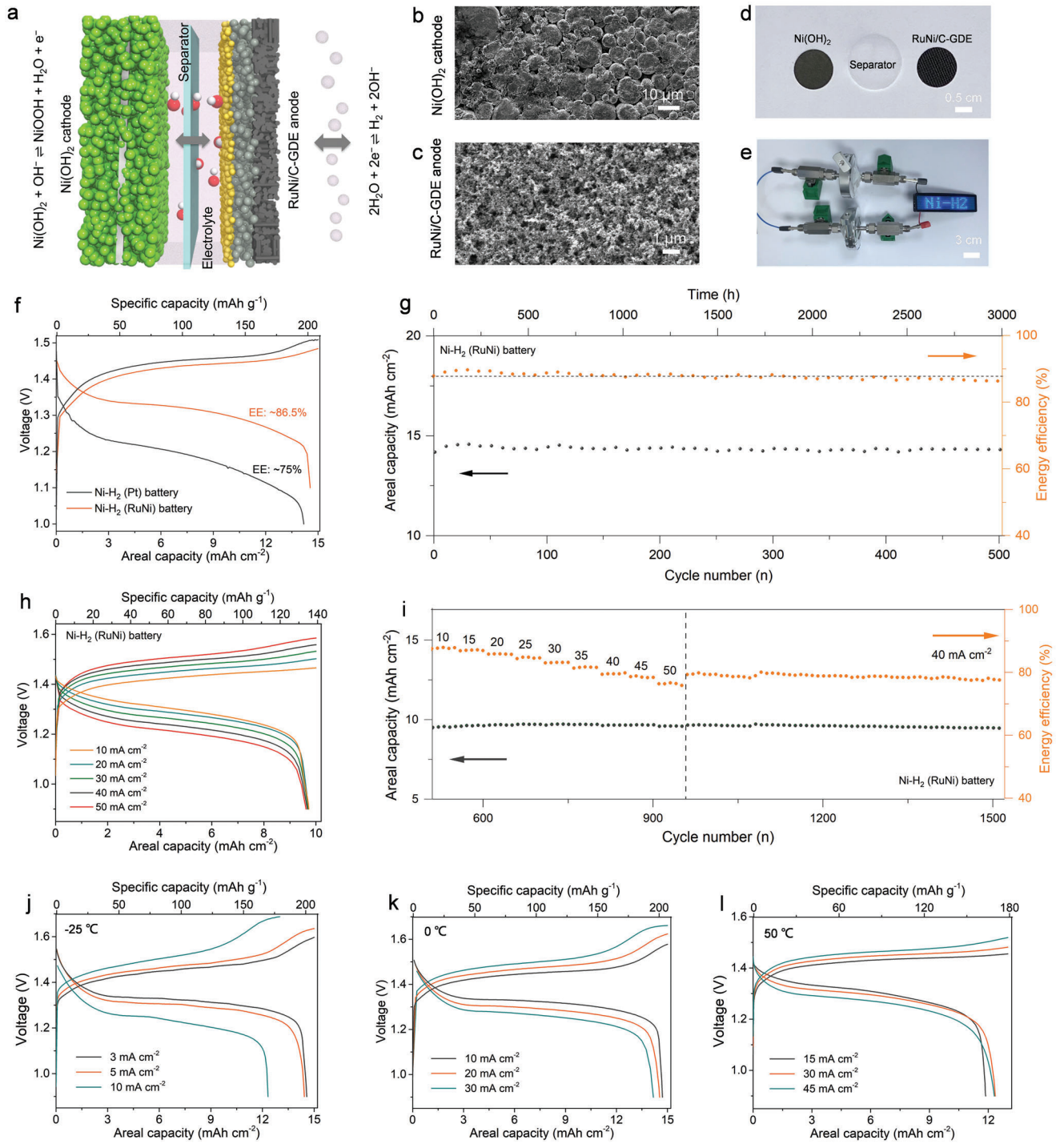

Figure 4. Electrochemical performance of the Ni-H_2 batteries. a) Schematic diagram of Ni–H_2 battery. SEM images of the surface of $Ni(OH)_2$ cathode (b) and H_2 anode (c). d) A digital photograph of commercial $Ni(OH)_2$ cathode, H_2 GDE, and separator with 26 wt.% KOH electrolyte. e) A digital photograph of Ni–H_2 Swagelok batteries for lighting an LED display screen. f) The galvanostatic charge–discharge curves of Ni–H_2 (RuNi) battery and Ni–H_2 (Pt) battery at 15 mA cm^{-2}. g) Cycle stability of the Ni–H_2 (RuNi) battery at a current density of 5 mA cm^{-2}. The rate performance of the Ni–H_2 (RuNi) battery at 66.7% DoD (h) and the corresponding cycling stability (i). Galvanostatic charge–discharge curves of the Ni–H_2 (RuNi) battery at different current densities and temperatures of −25 °C (j), 0 °C (k), and 50 °C (l).

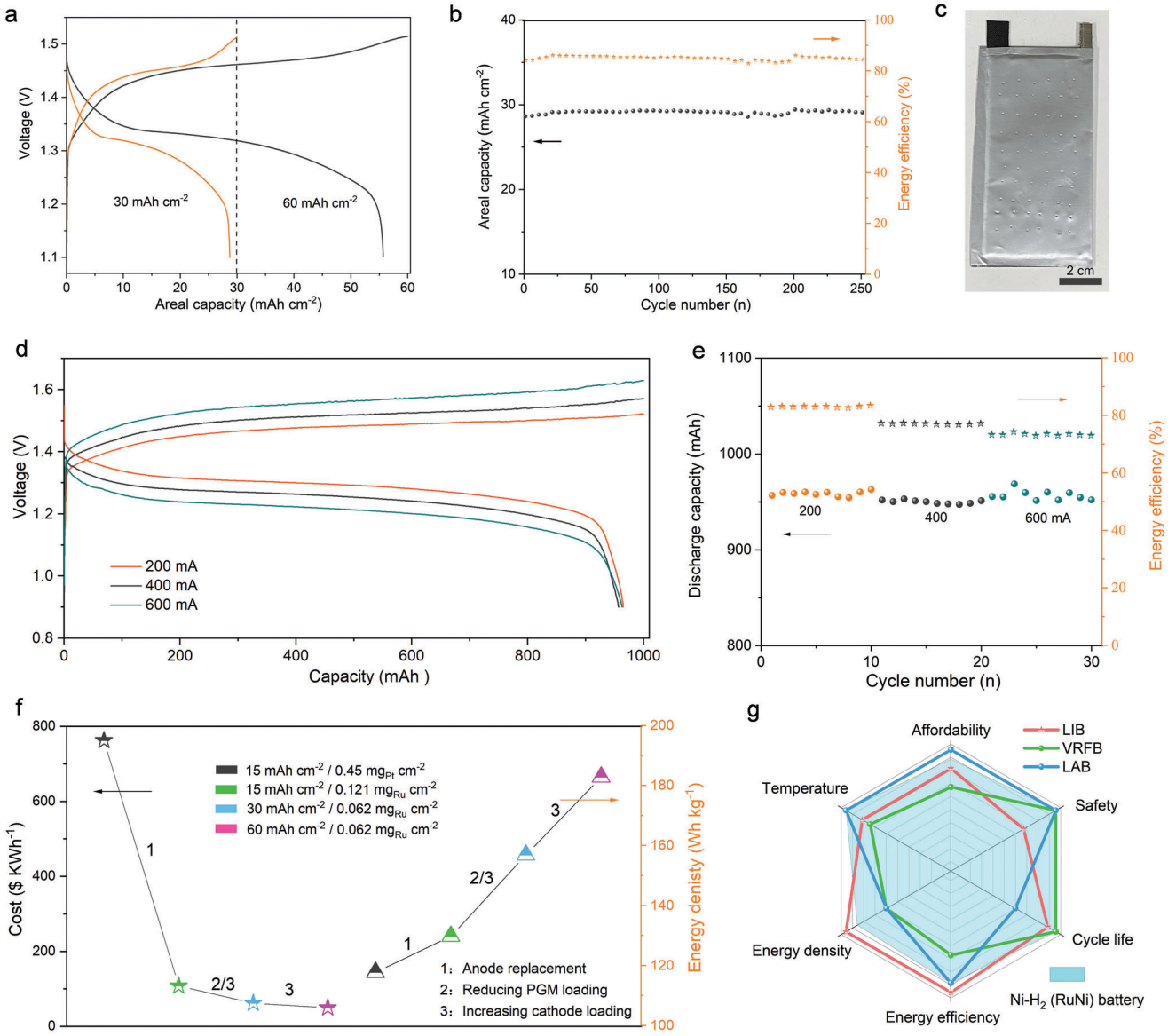

Figure 5. Electrochemical performances of Ni–H_2 batteries under high areal capacities. a) The galvanostatic charge-discharge curves of the Ni–H_2 (RuNi) battery with 30 mAh cm^{-2} and 60 mAh cm^{-2} at a current density of 5 mA cm^{-2}. b) The corresponding cycling stability of the Ni–H_2 (RuNi) battery with 30 mAh cm^{-2}. c) A digital photograph of a 1-Ah pouch-type Ni–H_2 battery (30 mAh cm^{-2}). d) The galvanostatic charge-discharge curves of the pouch-type Ni–H_2 (RuNi) battery at various current densities from 200 to 600 mA. e) The corresponding cycling stability and energy efficiency of the pouch-type Ni–H_2 (RuNi) battery. f) The cell stack energy density and cost of the Ni–H_2 (RuNi) battery compared with Ni–H_2 (Pt) battery. g) Performance comparison of the Ni–H_2 (RuNi) battery with LIB, VRFB, and LAB in terms of the key requirements of grid-scale energy storage, including affordability, safety, energy density, energy efficiency, all-climate adoptability, and cycle life.

Considering the high specific capacity and fast kinetics of the RuNi/C GDE anode, two Ni-H_2 batteries with higher areal capacities and lower Ru loadings of 62 μg_{Ru} cm^{-2} are assembled for demonstration (**Figure 5**a). The Ni-H_2 (RuNi) batteries with an ultrahigh cathode loading of 280 mg cm^{-2} (areal capacity of 60 mAh cm^{-2}) showed high energy efficiencies of ≈85% at 5 mA cm^{-2} and negligible decay of discharge capacity and energy efficiency after 50 cycles (Figure S17, Supporting Information). Besides, the Ni-H_2 (RuNi) batteries with a cathode loading of 140 mg cm^{-2} (areal capacity of 30 mAh cm^{-2}) also showed high energy efficiencies of ≈86.5% at 5 mA cm^{-2} and excellent durability after 250 cycles (Figure 5b). With the increase in capacity and reduce in catalyst loading, the cost proportion of the catalysts in the whole battery decreases significantly, reaching as low as ≈14.7% under 60 mAh cm^{-2} as compared to ≈47.6% under 15 mAh cm^{-2} and ≈22.8% under 30 mAh cm^{-2} (Figure S18, Supporting Information). The Ni-H_2 (RuNi) battery (60 mAh cm^{-2}) has an ultrahigh cell stack energy density of 183 Wh kg^{-1} and an attractive estimated cost of 49.1 $ kWh^{-1}, surpassing the United States Department of Energy (US DOE) target of 100 $ kWh^{-1} for large-scale energy storage applications (Table S4, Supporting Information).[7] For comparison, the Ni-H_2 (RuNi) battery

(30 mAh cm^{-2}) has a cell stack energy density of 152 Wh kg^{-1} and an estimated cost of 62 \$ kWh^{-1} (Table S5, Supporting Information). An Ah-level Ni-H_2 pouch cell was further assembled for practical energy storage applications (Figure 5c; Figure S19, Supporting Information). Excellent battery performance with an EE of ~84.5% can be obtained at a current density of 200 mA (Figure 5d,e). Therefore, it is rationalized to achieve high battery energy density and low battery cost by replacing the platinum catalyst with a low-cost ruthenium-based catalyst, further by reducing the amount of RuNi catalyst and increasing the cathode mass loading (Figure 5f).

Besides, it should be noted that the hydrogen pressure maintained in our prototype battery is less than 0.2 MPa, although it is verified that the battery shows better discharge performance under higher pressure (Figure S20, Supporting Information). In fact, the H_2 pressure in commercialized Ni-H_2 batteries is 1–2 orders of magnitude lower than that of the fuel cell H_2 tank with several tens of MPa, showing much less dependent of our batteries on the H_2 storage vessel with improved safety.[20] Based on the further optimized hydrogen gas pressure, electrode structure, and solid-liquid-gas three-phase interface,[21] the Ni-H_2 battery based on the RuNi/C catalyst is believed to show higher energy efficiency and lower cost.[9,22] In short, based on the low-cost and high-activity RuNi/C catalyst, the Ni-H_2 battery showed unprecedented comprehensive performance. Compared with the lithium-ion battery (LIB), vanadium redox-flow battery (VRFB), and lead-acid battery (LAB), which are the most promising battery technologies for grid-scale energy storage thus far, our advanced Ni-H_2 (RuNi) batteries showed all-around advantages with no obvious shortcoming in fulfilling the key requirements for grid-scale energy storage, including affordability, safety, energy density, energy efficiency, all-climate adoptability, and cycle life (Figure 5g).

3. Conclusion

In summary, low-cost and high-mass-activity electrocatalysts were synthesized by an ultrafast electrical pulse method for beyond-industrial-level Ni–H_2 batteries. This method demonstrated extremely high energy conversion efficiency with ultrashort synthesis duration of ≈0.5 s. The synthesized RuNi nanoparticles of ≈3 nm were uniformly and tightly anchored onto the carbon substrates, which displayed excellent HER/HOR performance in alkaline electrolytes with a catalyst cost of ≈1/5 that of commercial Pt/C, for example a low HER overpotential of 19.5 mV at a current density of 10 mA cm^{-2} and a high HOR mass activity of 2.34 A mg^{-1}. The remarkable HER/HOR activities of the RuNi nanocatalysts were confirmed by the DFT theoretical calculations, revealing that the Ni alloying optimized the electronic structure of Ru and accelerated the RDS of the HER/HOR. Advanced Ni–H_2 batteries based on the low-cost RuNi/C catalysts achieved high energy efficiency (>85%), high cell stack energy density of 183 Wh kg^{-1}, well-maintained performance in the all-climate temperature range (−25–50 °C), and excellent durability with negligible energy efficiency decay. In addition, the estimated cost of the cell stack reaches as low as ≈49.1 \$ kWh^{-1}, superior to the US DOE target of 100 \$ kWh^{-1} for large-scale energy storage applications. This work provides opportunities to the exploration of practical beyond-industrial-level hydrogen gas batteries for grid-scale energy storage.

4. Experimental Section

Pretreatment of the Carbon Black: First, 5 g carbon black (Vulcan XC-72, Fuel Cell Store) was dispersed in 250 mL concentrated nitric acid, and then the reaction vessel was placed in an oil bath at 80 °C under reflux for 5 h. After cooling to room temperature, the reaction mixture was poured into deionized water, and the precipitants, oxidized carbon black, were collected by suction filtration.

Synthesis of RuNi/C: The Ru/Ni ratio of the obtained RuNi/C can be controlled by the ratio of the Ru and Ni metal sources. First, actived carbon black (CB) was mixed with metal salt precursors by fully immersing 12 mg CB into 0.3 mL 0.03 M $RuCl_3 \cdot 3H_2O$ (Sigma–Aldrich) and 0.02 M $Ni(NO_3)_2 \cdot 6H_2O$ (Sigma–Aldrich) mixed aqueous solution. After drying, the CB coating with metal salts was placed between two tightly attached carbon cloths (1 cm × 2 cm) to conduct the ultrafast electrical pulse treatment. The high temperature rapidly decomposed these precursor salts into metal nanoparticles to anchor on the carbon black and then cooled rapidly to prevent nanoparticle agglomeration. The current pulse flowing through the carbon cloths was 20 A for ≈0.5 s. The resulting RuNi/C was then collected and stored in the oven for testing.

Materials Characterization: X-ray diffraction patterns were collected on a Philips X'Pert PRO SUPER X-ray diffractometer equipped with Cu K_α radiation in a 2θ range of 30°–90°. Transmission electron microscopy (JEM-F200) and energy-dispersive spectral mapping images were employed to visualize the morphologies and element distribution of the samples. The chemical states of the samples were analyzed by X-ray photoelectron spectroscopy (Kratos Axis supra$^+$). The ICP–OES results were taken by an Optima 7300 DV instrument. Thermogravimetry (TG) analysis of the samples was carried out on a NETZSCH TG 209F1 Libra instrument at a heating rate of 10 °C min^{-1} from 25 to 800 °C in an air atmosphere.

Electrocatalytic Measurements: The electrocatalytic measurements were conducted on a VMP-3 multichannel workstation (Bio-Logic Science Instruments, France) with a three-electrode system. The catalyst-loaded RDE (5 mm diameter, Pine Instruments, USA) or GDE (1 cm^2) was used as the working electrode, and the Ag/AgCl electrode and graphite rod were used as the reference electrode and counter electrode, respectively. The electrolyte for the HER tests was Ar-saturated 1.0 M KOH, and the electrolyte for the HOR tests was high-purity H_2-saturated 0.1 M KOH. The catalyst inks of RuNi/C, Ru/C (20% Ru on Vulcan XC-72, Premetek, USA), and Pt/C (20% Pt on Vulcan XC-72, Premetek, USA) of ≈10 $\mu g_{cat.}$ cm^{-2} were prepared by dispersing the catalysts in water/ethanol (1:3, v/v) with Nafion (5 wt.%) under ultrasound sonication. The ink was drop-casted on the glassy carbon (GC) electrode to form a homogeneous catalyst film. The LSV curves of HER and HOR were collected at a scan rate of 5 mV s^{-1}. All LSV polarization curves for HER and HOR were iR-corrected ($E_{corrected} = E_{measured} - iR_s$). The catalysts and polyvinylidene fluoride (PVDF) binder with a mass ratio of 9:1 was coated on a gas diffusion layer (GDL) for the H_2 GDE tests. The exchange current density (j_0) can be calculated by fitting j_k into the B–V equation in the micro-polarization region.

Battery Performance Measurements: The electrochemical properties of the batteries were measured using Swagelok cells and cylindrical testing cells, which were reported in previous studies.[7a] A polymer separator (FS2225-33, Freudenberg Performance Materials SE & Co. KG) wetted with 26 wt.% KOH electrolyte was used between the H_2 anode and $Ni(OH)_2$ cathode (Hunan Corun New Energy Co., Ltd.). The symmetrical H_2 cell was fabricated by using the catalyst coated GDL as both positive and negative electrodes. The cell performance of the batteries was tested on a VMP-3 multichannel workstation (Bio-Logic Science Instruments, France) and battery test systems (LandHe and Neware).

DFT Calculations: DFT calculations were carried out using the Vienna ab initio Simulation Package (5.4.4 VASP) within the generalized gradient approximation (GGA) as formulated by the Perdew–Burke–Ernzerhof (PBE) functional.[23] To avoid interaction from nearby layers, different

surfaces with nine atom layers of Ru (101) and RuNi (101) were modeled with a 20 Å vacuum space. The final set of energies for all calculations was computed with an energy cutoff of 520 eV. The convergence criteria for energy were set to 10^{-5} eV, and the residual forces on each atom were decreased by more than 0.02 eV $Å^{-1}$. Brillouin zone integration was performed with $2 \times 3 \times 1$ Γ-centered Monkhorst-Pack k-point meshes for geometry optimization calculations. All the isosurface values for the charge density difference analysis were set to 0.003 eV $Å^{-3}$, and cyan and yellow colors represent the charge depletion and charge accumulation zones, respectively. The free energy results of the HER/HOR process were obtained by referring to the computational hydrogen electrode (CHE) model proposed by Nørskov et al.[24] The minimum kinetic energy barrier of water dissociation was obtained by means of the climbing image nudged elastic band (CI-NEB) method.[25]

Supporting Information

Supporting Information is available from the Wiley Online Library or from the author.

Acknowledgements

T.L.J. and Z.C.L. contributed equally to this work. W.C. acknowledges the support from the Fundamental Research Funds for the Central Universities (Grant KY2060000150, WK2060000040). This work was also supported by the Joint Laboratory for USTC and Yanchang Petroleum (2022ZK-03). The authors would like to thank the technical support from the USTC Center for Micro and Nanoscale Research and Fabrication, and the advanced computing resources provided by the Supercomputing Center of the USTC.

Conflict of Interest

The authors declare no conflict of interest.

Data Availability Statement

Research data are not shared.

Keywords

all-climate performance, electrical pulse synthesis, grid-scale energy storage, HER/HOR catalysts, hydrogen gas batteries, long life

Received: January 16, 2023
Revised: May 13, 2023
Published online: June 29, 2023

[1] a) O. Schmidt, S. Melchior, A. Hawkes, I. Staffell, *Joule* **2019**, *3*, 81; b) N. Kittner, F. Lill, D. M. Kammen, *Nat. Energy* **2017**, *2*, 17125; c) W. A. Braff, J. M. Mueller, J. E. Trancik, *Nat. Clim. Change* **2016**, *6*, 964; d) Z. G. Yang, J. L. Zhang, M. C. W. Kintner-Meyer, X. C. Lu, D. W. Choi, J. P. Lemmon, J. Liu, *Chem. Rev.* **2011**, *111*, 3577; e) B. Dunn, H. Kamath, J. M. Tarascon, *Science* **2011**, *334*, 928; f) Z. Zhu, T. Jiang, M. Ali, Y. Meng, Y. Jin, Y. Cui, W. Chen, *Chem. Rev.* **2022**, *22*, 16610.

[2] a) D. Larcher, J. M. Tarascon, *Nat. Chem.* **2015**, *7*, 19; b) G. J. May, A. Davidson, B. Monahov, *J. Energy Storage* **2018**, *15*, 145; c) Y. Morioka, S. Narukawa, T. Itou, *J. Power Sources* **2001**, *100*, 107; d) H. L. Pan, Y. S. Hu, L. Q. Chen, *Environ Sci* **2013**, *6*, 2338; e) E. Sanchez-Diez, E. Ventosa, M. Guarnieri, A. Trovo, C. Flox, R. Marcilla, F. Soavi, P. Mazur, E. Aranzabe, R. Ferret, *J. Power Sources* **2021**, *481*, 228804; f) P.-J. Tsais, L. Chan, *Electricity Transmission, Distribution and Storage Systems* **2013**, *309*, https://doi.org/10.1533/9780857097378.3.309; g) L. Z. Fan, H. C. He, C. W. Nan, *Nat. Rev. Mater.* **2021**, *6*, 1003; h) T. L. Jiang, P. G. He, G. X. Wang, Y. Shen, C. W. Nan, L. Z. Fan, *Adv. Energy Mater.* **2020**, *10*, 1903376; i) Z. N. Li, T. L. Jiang, M. Ali, C. X. Wu, W. Chen, *Energy Storage Mater.* **2022**, *50*, 105.

[3] a) Y. Cao, M. Li, J. Lu, J. Liu, K. Amine, *Nat. Nanotechnol.* **2019**, *14*, 200; b) M. Ue, K. Sakaushi, K. Uosaki, *Mater. Horiz.* **2020**, *7*, 1937; c) L. Li, Q. Zhang, B. He, R. Pan, Z. Wang, M. Chen, Z. Wang, K. Yin, Y. Yao, L. Wei, *Adv. Mater.* **2021**, *34*, 2104327.

[4] a) D. K. Coates, B. K. Grindstaff, P. S. Hoofnagle, D. P. Chiappetti, *Capacitors and Fuel Cells* **1995**, *393*, 257; b) D. B. Caldwell, D. K. Coates, C. L. Fox, L. E. Miller, Space Technology and Applications International Forum (Staif-96), *Pts 1–3* **1996**, 199.

[5] a) A. H. Zimmerman, J. Matsumoto, T. Poston, A. Prater, T. Barrera, *Proceedings of the 34th Int. Power Sources Symp.*, IEEE, Cherry Hill, NJ, USA **1990**, 246; b) H. Vaidyanathan, *J. Power Sources* **1988**, *22*, 221.

[6] a) B. Liu, X. R. Liu, X. Y. Fan, J. Ding, W. B. Hu, C. Zhong, *J. Alloys Compd.* **2020**, *834*, 155185; b) H. L. Wang, Y. Y. Liang, M. Gong, Y. G. Li, W. Chang, T. Mefford, J. G. Zhou, J. Wang, T. Regier, F. Wei, H. J. Dai, *Nat. Commun.* **2012**, *3*, 917; c) W. H. Zhou, D. Zhu, J. He, J. C. Li, H. Chen, Y. G. Chen, D. L. Chao, *Environ Sci* **2020**, *13*, 4157.

[7] a) W. Chen, Y. Jin, J. Zhao, N. Liu, Y. Cui, *Proc. Natl. Acad. Sci. USA* **2018**, *115*, 11694; b) T. Jiang, W. Chen, *Curr. Opin. Electrochemi.* **2021**, *30*, 100859; c) T. Jiang, K. Li, S. Park, K. Zheng, Y. Meng, Y. Yuan, Z. Liu, Z. Zhu, X. Zheng, S. Liu, W. Chen, *Nano Lett.* **2022**, *4*, 1741; d) Z. Liu, J. Yang, F. Wang, Y. Yuan, T. Jiang, Z. Zhu, K. Li, S. Liu, K. Zhang, W. Wang, M. Chuai, J. Sun, Y. Wu, W. Chen, *Nano Lett.* **2022**, *22*, 7860.

[8] a) Z. X. Zhu, Y. H. Meng, Y. Cui, W. Chen, *Adv. Funct. Mater.* **2021**, *31*, 2101024; b) Z. Zhu, Y. Meng, Y. Yin, Z. Liu, T. Jiang, Q. Peng, T. Yin, M. Li, W. Chen, *Energy Storage Mater.* **2021**, *42*, 464; c) Z. X. Zhu, M. M. Wang, Y. H. Meng, Z. H. Lin, Y. Cui, W. Chen, *Nano Lett.* **2020**, *20*, 3278; d) W. Chen, G. D. Li, A. Pei, Y. Z. Li, L. Liao, H. X. Wang, J. Y. Wan, Z. Liang, G. X. Chen, H. Zhang, J. Y. Wang, Y. Cui, *Nat. Energy* **2018**, *3*, 428; e) J. Zheng, W. C. Sheng, Z. B. Zhuang, B. J. Xu, Y. S. Yan, *Sci. Adv.* **2016**, *2*, e1501602.

[9] a) L. H. Thaller, A. H. Zimmerman, G. A. To, *J. Power Sources* **2003**, *114*, 309; b) E. S. Liu, L. Jiao, J. K. Li, T. Stracensky, Q. Sun, S. Mukerjee, Q. Y. Jia, *Environ Sci* **2020**, *13*, 3064; c) W. C. Sheng, M. Myint, J. G. G. Chen, Y. S. Yan, *Environ Sci* **2013**, *6*, 1509; d) X. Yang, J. Nash, N. Oliveira, Y. S. Yan, B. Xu, *Angew. Chem., Int. Ed.* **2019**, *58*, 17718; e) J. Zheng, W. C. Sheng, Z. B. Zhuang, B. J. Xu, Y. S. Yan, *Sci. Adv.* **2016**, *2*, 1501602; f) D. Strmcnik, M. Uchimura, C. Wang, R. Subbaraman, N. Danilovic, D. van der Vliet, A. P. Paulikas, V. R. Stamenkovic, N. M. Markovic, *Nat. Chem.* **2013**, *5*, 300.

[10] Z. H. Zhou, Y. J. Liu, J. H. Zhang, H. Pang, G. X. Zhu, *Electrochem. Commun.* **2020**, *121*, 106871.

[11] E. S. Davydova, F. D. Speck, M. T. Y. Paul, D. R. Dekel, S. Cherevko, *ACS Catal.* **2019**, *9*, 6837.

[12] a) Y. Y. Zhou, Z. Y. Xie, J. X. Jiang, J. Wang, X. Y. Song, Q. He, W. Ding, Z. D. Wei, *Nat. Catal.* **2020**, *3*, 454; b) J. Mahmood, F. Li, S. M. Jung, M. S. Okyay, I. Ahmad, S. J. Kim, N. Park, H. Y. Jeong, J. B. Baek, *Nat. Nanotechnol.* **2017**, *12*, 441; c) Y. M. Zhao, X. W. Wang, G. Z. Cheng, W. Luo, *ACS Catal.* **2020**, *10*, 11751; d) D. H. Kweon, M. S. Okyay, S. J. Kim, J. P. Jeon, H. J. Noh, N. Park, J. Mahmood, J. B. Baek, *Nat. Commun.* **2020**, *11*, 1278; e) Y. Liu, X. Li, Q. H. Zhang, W. D. Li, Y. Xie, H. Y. Liu, L. Shang, Z. Y. Liu, Z. M. Chen, L. Gu, Z. Y. Tang, T. R. Zhang, S. Y. Lu, *Angew. Chem., Int. Ed.* **2020**, *59*, 1718.

[13] a) Y. R. Xue, L. Shi, X. R. Liu, J. J. Fang, X. D. Wang, B. P. Setzler, W. Zhu, Y. S. Yan, Z. B. Zhuang, *Nat. Commun.* **2020**, *11*, 5651; b) M. Y. Yuan, C. Wang, Y. Wang, Y. Wang, X. M. Wang, Y. K. Du, *Nanoscale* **2021**, *13*, 13042; c) M. X. Li, H. Y. Wang, W. D. Zhu, W. M. Li, C. Wang, X. F. Lu, *Adv. Sci.* **2020**, *7*, 1901833; d) G. X. Lin, Y. D. Wang, J. Hong,

K. Suenaga, L. J. Liu, L. Y. Chang, C. W. Pao, T. Zhang, W. Zhao, F. Q. Huang, M. H. Yang, Y. Y. Sun, J. C. Wang, *ChemSusChem* **2020**, *13*, 2739; e) Q. Yuan, Y. Yang, S. P. Gong, S. Chen, M. X. Huang, C. L. Wang, H. G. Tong, Q. W. Chen, *Chinese J. Chem* **2021**, *39*, 3455; f) L. L. Han, P. F. Ou, W. Liu, X. Wang, H. T. Wang, R. Zhang, C. W. Pao, X. J. Liu, W. F. Pong, J. Song, Z. B. Zhuang, M. V. Mirkin, J. Luo, H. L. L. Xin, *Sci. Adv.* **2022**, *8*, 3779.

[14] a) X. L. Tian, X. Zhao, Y. Q. Su, L. J. Wang, H. M. Wang, D. Dang, B. Chi, H. F. Liu, E. J. M. Hensen, X. W. Lou, B. Y. Xia, *Science* **2019**, *366*, 850; b) M. C. Luo, Z. L. Zhao, Y. L. Zhang, Y. J. Sun, Y. Xing, F. Lv, Y. Yang, X. Zhang, S. Hwang, Y. N. Qin, J. Y. Ma, F. Lin, D. Su, G. Lu, S. J. Guo, *Nature* **2019**, *574*, 81; c) C. H. Zhan, Y. Xu, L. Z. Bu, H. Z. Zhu, Y. G. Feng, T. Yang, Y. Zhang, Z. Q. Yang, B. L. Huang, Q. Shao, X. Q. Huang, *Nat. Commun.* **2021**, *12*, 6261.

[15] a) Y. Qiao, Y. G. Yao, Y. Liu, C. J. Chen, X. Z. Wang, G. Zhong, D. P. Liu, L. B. Hu, *Small* **2020**, *16*, 2000509; b) Y. Qiao, C. J. Chen, Y. Liu, Y. F. Liu, Q. Dong, Y. G. Yao, X. Z. Wang, Y. Y. Shao, C. Wang, L. B. Hu, *Nano Lett.* **2021**, *21*, 4517; c) S. L. Liu, Z. Hu, Y. Z. Wu, J. F. Zhang, Y. Zhang, B. H. Cui, C. Liu, S. Hu, N. Q. Zhao, X. P. Han, A. Y. Cao, Y. N. Chen, Y. D. Deng, W. B. Hu, *Adv. Mater.* **2020**, *32*, 2006034; d) Y. G. Yao, Z. N. Huang, P. F. Xie, S. D. Lacey, R. J. Jacob, H. Xie, F. J. Chen, A. M. Nie, T. C. Pu, M. Rehwoldt, D. W. Yu, M. R. Zachariah, C. Wang, R. Shahbazian-Yassar, J. Li, L. B. Hu, *Science* **2018**, *359*, 1489; e) D. X. Luong, K. V. Bets, W. A. Algozeeb, M. G. Stanford, C. Kittrell, W. Chen, R. V. Salvatierra, M. Q. Ren, E. A. McHugh, P. A. Advincula, Z. Wang, M. Bhatt, H. Guo, V. Mancevski, R. Shahsavari, B. I. Yakobson, J. M. Tour, *Nature* **2020**, *577*, 647.

[16] X. Y. Tian, P. C. Zhao, W. C. Sheng, *Adv. Mater.* **2019**, *31*, 1808066.

[17] a) X. Guo, X. Wan, Q. Liu, Y. Li, W. Li, J. Shui, *eScience* **2022**, *2*, 304; b) T. Wang, X. Cao, L. Jiao, *eScience* **2021**, *1*, 69; c) Z. Li, W. Wang, Q. Qian, Y. Zhu, Y. Feng, Y. Zhang, H. Zhang, M. Cheng, G. Zhang, *eScience* **2022**, *2*, 416.

[18] X. Liu, Y. Jiao, Y. Zheng, K. Davey, S. Z. Qiao, *J. Mater. Chem. A* **2019**, *7*, 3648.

[19] a) H. S. Lim, S. A. Verzwyvelt, *J. Power Sources* **1990**, *29*, 503; b) H. S. Lim, S. A. Verzwyvelt, *J. Power Sources* **1988**, *22*, 213.

[20] M. X. Li, Y. F. Bai, C. Z. Zhang, Y. X. Song, S. F. Jiang, D. Grouset, M. J. Zhang, *Int. J. Hydrogen Energy* **2019**, *44*, 10677.

[21] a) H. S. Jiang, R. H. Luo, Y. M. Li, W. Chen, *Ecomat* **2022**, *4*, e12199; b) T. L. Jiang, S. Y. Wei, L. X. Li, K. Zheng, X. H. Zheng, S. Park, S. Liu, Z. X. Zhu, Z. C. Liu, Y. H. Meng, Q. Peng, Y. C. Feng, W. Chen, *ACS Nano* **2023**, *17*, 7821.

[22] a) A. Visintin, A. Anani, S. Srinivasan, A. J. Appleby, H. S. Lim, *J. Appl. Electrochem.* **1995**, *25*, 833; b) D. B. Caldwell, C. L. Fox, L. E. Miller, *J. Power Sources* **1997**, *65*, 23; c) G. Rao, H. Vaidyanathan, *Proc. Iecec* **1996**, 384, https://doi.org/10.1109/IECEC.1996.552912.

[23] a) G. Kresse, J. Furthmuller, *Phys. Rev. B* **1996**, *54*, 11169; b) J. P. Perdew, K. Burke, M. Ernzerhof, *Phys. Rev. Lett.* **1996**, *77*, 3865; c) J. P. Perdew, Y. Wang, *Phys. Rev. B* **1992**, *45*, 13244; d) S. Grimme, J. Antony, S. Ehrlich, H. Krieg, *J. Chem. Phys.* **2010**, *132*, 154104.

[24] J. K. Norskov, T. Bligaard, A. Logadottir, J. R. Kitchin, J. G. Chen, S. Pandelov, J. K. Norskov, *J. Electrochem. Soc.* **2005**, *152*, J23.

[25] G. Henkelman, B. P. Uberuaga, H. Jonsson, *J. Chem. Phys.* **2000**, *113*, 9901.